



Analytical and Numerical Modeling of the Effect of Variable Flow Boundaries on the Squeeze Film Behavior in MEMS

A. Roychowdhury^{1,2}, S. Patra³, A. Nandy¹, R. Pratap^{1,2}

¹Dept. of Mechanical Engineering, Indian Institute of Science Bangalore, ²Center for Nano Science and Engineering, Indian Institute of Science Bangalore, ³Dept. of Mechanical Engineering,

Jadavpur University Kolkata,

*Corresponding author:

anish.roychowdhury@gmail.com

Keywords:

Squeeze film,
Flow boundaries,
Elastic micro-plate,
FEM coupled.

Abstract

We analyze the forces produced by a thin fluid film (called squeeze film) present between an oscillating elastic rectangular micro-plate and a fixed substrate under different practical flow boundary conditions. The plate is fixed along its edges and is assumed to vibrate in its first fundamental mode. The fluid underneath is squeezed differently depending on the side venting condition. We derive analytical expressions for the squeeze film damping and spring forces for different flow boundary conditions – all sides open (OOOO), all sides closed (CCCC), adjacent sides open (OOC), etc. The derivation is illustrated considering the all sides open case results. We then discuss the results for different flow boundary conditions. We find that restricting the fluid flow along the three edges compared to the all sides open case results in as much as 45 times increase in the squeeze film induced stiffness and six times increase in the peak damping. These results indicate the use of boundary venting conditions as an additional design parameter for controlling damping and ; hence, Q as well as the squeeze film stiffness. We verify our analytical results with a FORTRAN simulation data based on a finite element methodology. The numerical results show a good agreement with the analytical solutions.

1. Introduction

1.1 Motivation

MEMS devices like gyroscopes, micro-mirrors, acoustic transducers, etc., often consist of a vibrating plate-like structure with a thin air film trapped in a micron or sub-micron scale gap. Under such conditions, the trapped air acts like a squeeze film offering a pressure force on the bottom surface of the plate thus opposing its motion. As a consequence, the air film acts as a damper and is responsible for reducing the Q factor of the device. This phenomenon is known as

the squeeze film damping. This damping is generally modeled by the Reynolds equation, which is derived from the Navier Stokes equation by incorporating certain assumptions [Langlois (1962), Blech (1983)].

Prior work in this area includes studies on both rigid as well as flexible rectangular plates, with a varying structural and flow boundary conditions. These studies analyze the spring and the damping forces for normal as well as torsional plate motions [Pandey et al.(2007), Mohite (2007)]. Analytical expressions for the pressure and the reaction forces for rigid plates with different venting conditions was reported by [Darling et al. (1998)]. [Pandey et al. (2007)] discussed the effect of

partially blocked boundaries providing an analytical as well as a numerical simulation results for MEMS torsion mirrors. [Kumar (2010)] studied analytically the effect of varying flow boundaries on the squeeze film parameters using a Greens function approach proposed by [Darling et al. (1998)]. Kumar also discussed the effect of the ratio of the plate length to the air gap thickness on the damping coefficient, when different flow boundary conditions were considered. The change in stiffness with a variation in venting conditions at different squeeze numbers, using mode shapes for flexible plates in accordance with the flow boundary conditions is also reported. [Darling et al.(1998)] in their study of closed cavities demonstrated that the reaction force due to the trapped air inside the cavity remains in phase with displacement, for all frequencies resulting in pure spring force and no damping. The plate flexibility was not accounted in this study. [Ahmad and Pratap (2011)] concluded from an analytical study, solving the linearized Reynolds equation for the pressure distribution; that the reaction force thus obtained for a closed cavity remains completely in phase with displacement; with no viscous damping even when the flexibility of the plate is considered. [Kumar (2010)] also studied the all sides closed structural and flow boundary conditions using a numerical ANSYS FLOTRAN simulation and found the presence of damping for larger plate length to air gap-ratios. In another work, [Altug and Rao (2010)] presented an analytical technique for the flexible plates by taking the non-linear form of the Reynolds equation and treating the pressure distribution as a series sum of harmonics. They concluded from the analytical expressions that a non zero damping force exists for the all sides closed flow boundary condition due to the pumping mechanism resulting from the mode shape. The above mentioned studies report on the spring and the damping forces for the closed cavities and varying open boundaries, which are in accordance with the structural boundary conditions. In all of these works; however, the flow boundary conditions are not decoupled from the structural boundary condition, except for the classic closed cavity case.

It is important to understand the distinction between the structural boundary conditions for the vibrating micro-mechanical structure, and the flow boundary conditions for the squeeze film. The natural frequencies and the mode shapes of the vibrating structure are affected by how the plate is clamped on its sides. The flow or venting boundary conditions for the squeeze film dictate the pressure distribution in the squeezed film region. Typically, a monolith fabrication process such as the surface micromachining results in a structure, where the two boundary conditions are inseparable. For example, releasing a cantilever

beam results in venting (i.e. zero differential pressure) flow boundary conditions on the three free sides

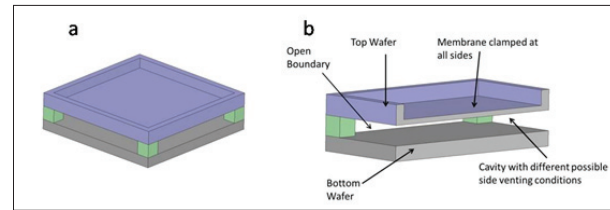


Figure 1: Schematic of the flexible MEMS microplate (all sides opened) (a) isometric view (b) sectional view.

of the cantilever. Thus, the flow boundary conditions are coupled to the structural boundary conditions and mode shapes. It is, however, possible to uncouple these two by using, say, a wafer bonding process, where the vibrating structure is realized in one wafer and the squeeze film cavity in another wafer as shown in Fig. 1. This kind of fabrication decouples the two boundary conditions and one can easily have an all sides clamped plate vibrating in a cavity with an all sides open flow boundaries. This uncoupling allows for an independent engineering of the fluid flow conditions thus, providing a separate control for manipulating the Q of the structure.

This is of significant practical application, where it is not desirable to have holes in the membrane such as in the case of the acoustic transducers. When the membrane vibrates, the air-flow in the lower cavity is subjected to different flow boundary conditions along the edges of this cavity depending on the bonding area geometry. It is possible to design bonding along the perimeter in such a way that different sides are closed or open, e.g., two opposite sides open or two adjacent sides open. The flow induced damping, therefore, naturally depends on the venting conditions. We thus observe the importance of the flow boundary conditions and the study of the same is important for the proper understanding of a variation in the squeeze film damping parameters which, in turn, can affect the Q factor, and also change the dynamic characteristics of the device.

1.2 Contribution of the current work

In this work, we have studied the effect of varying the flow boundary on the squeeze film damping and the stiffness. We decoupled the structural and flow boundary conditions by considering an all sides fixed plate, which has variable flow boundaries. We found out that by changing the flow boundaries one can tune the dynamic characteristics of the resonant MEMS devices. We developed analytical expressions using an eigen expansion technique for the squeeze film stiffness and damping, for all possible combinations of the open and the closed flow boundaries for a rectangular plate clamped at all edges. An assumed first mode shape satisfying the kinematic

boundary condition is used to accommodate the effect of plate flexibility. The variations of pressure and phase angle are studied along with the resulting stiffness and damping for a range of squeeze numbers. A comparative study of the stiffness and the damping offered by each of the flow boundary conditions is presented. We have provided physical explanations for the differences in behavior as observed from the analytical study, for each of the flow boundary conditions. In order to validate our analytical expressions, we had compared our analytical results with a numerically simulated data generated from a FORTRAN code, using a finite element methodology described in detail in our prior work [Roychowdhury et al. (2013)]. The numerical simulation results show a good agreement with our analytical results.

2 Mathematical formulation

2.1 Governing equation

The governing equations for the squeeze film flow are derived from the standard Navier Stokes equation using the continuity equation and appropriate assumptions on isothermal conditions, pressure invariance across the film thickness, etc. The derivation is available in many references (for eg., see [Kumar (2010)]. The resulting governing equation is the Reynolds equation given by

$$\frac{\partial}{\partial x} \left(\frac{ph^3}{\mu} \frac{\partial p}{\partial x} \right) + \frac{\partial}{\partial y} \left(\frac{ph^3}{\mu} \frac{\partial p}{\partial y} \right) = 12 \frac{\partial(ph)}{\partial t} \quad (1)$$

where ‘ p ’ is the pressure, ‘ h ’ is the air gap, and ‘ μ ’ is the viscosity of the air. A linearization of Eq. 1 under the assumptions of small amplitude motion $h = h_a + \hat{h}$ (‘ h_a ’ is the initial air gap and ‘ \hat{h} ’ is the perturbation in the air gap), small pressure $p = p_a + \hat{p}$ (‘ p_a ’ perturbations is the ambient pressure and ‘ \hat{p} ’ is the pressure perturbation) and the use of normalized variables for pressure, film thickness as $P = \frac{\hat{p}}{p_a}$, $H = \frac{\hat{h}}{h_a}$, leads to the following form of the governing equation,

$$\nabla^2 P - \alpha^2 \frac{\partial P}{\partial t} = \alpha^2 \frac{\partial H}{\partial t} \quad (2)$$

where ‘ α ’ is a constant ($\alpha = \sqrt{\frac{12\mu}{h_a^2 p_a}}$), and ‘ L ’ and ‘ W ’ are the plate length and the width respectively.

2.2 Solution using the eigen expansion method

We solved the linearized Reynolds equation given by (2) using the eigen functions for the spatial variation of pressure. We carried out an eigen function analysis on the homogeneous form of Eq. 1. Let $P = \sum_{m,n} f_{mn}(x,y)T(t)$, where the sum indicates a linear combination of the

eigen functions $\Psi_{mn}(x,y)$ with $f_{mn} = a_{mn}\Psi_{mn}(x,y)$, $\Psi_{mn}(x,y)$ being an eigen function, a_{mn} a scalar coefficient and $T(t)$ being the temporal component of pressure. Substituting this expression for ‘ P ’ in the homogeneous form of Eq. 2 and using the separation of variables, we get

$$\frac{\nabla^2 f}{f} = \frac{\alpha^2}{T} \frac{\partial T}{\partial t} = -k_{mn}^2 \quad (3)$$

where k_{mn} is a constant corresponding to each f_{mn} . We can decouple k_{mn} for the two independent indices m and n by assuming:

$$k_{mn}^2 = k_m^2 + k_n^2 \quad (4)$$

On further assuming $\Psi_{mn}(x,y) = X_m(x)Y_n(y)$, and substituting in Eq. 3 we found out some more simplifications:

$$\Psi_{mn}(x,y) = \sin\left(\frac{m\pi x}{L}\right) \sin\left(\frac{n\pi y}{W}\right) \quad (5)$$

Assuming harmonic source term $H = \delta\phi e^{i\omega t}$, (where ‘ δ ’ is the vibration amplitude, ‘ ϕ ’ is the assumed first mode shape ($\phi = \sin(\frac{\pi x}{L}) \sin(\frac{\pi y}{W})$), and ‘ ω ’ is the oscillation frequency), and using the expression for Ψ_{mn} in the expression for pressure and using the orthogonality of the eigen functions we have determined the coefficient a_{mn}

$$a_{mn} = \delta \frac{\int_0^L \int_0^W i\omega\alpha^2 \phi \Psi_{mn} dy dx}{\int_0^L \int_0^W [-k_{mn}^2 - i\omega\alpha^2] \Psi_{mn}^2 dy dx} \quad (6)$$

Now the pressure is given by

$$P = \sum a_{mn} \Psi_{mn}(x,y) T(t) = \bar{P} T(t), \quad (7)$$

where ‘ \bar{P} ’ is the spatial component of the pressure.

For the all sides open boundaries, we have used zero pressure boundary conditions, $P(0,y)=P(L,y)=P(x,0)=P(x,W)=0$, and obtained the following expressions for the non dimensional quantities; P (pressure), F_s (stiffness force), and F_d (damping force).

$$P = -64\delta \sum_{m,n \in \text{odd}} \frac{[i\pi^2\sigma(m^2\beta^2 + n^2) + \sigma^2] \sin\left(\frac{m\pi x}{L}\right) \sin\left(\frac{n\pi y}{W}\right)}{[\pi^4(m^2\beta^2 + n^2)^2 + \sigma^2] m n \pi^2 (m^2 - 4)(n^2 - 4)} \quad (8)$$

$$F_s = \frac{-256\delta\sigma^2}{\pi^4} \sum_{m,n \in \text{odd}} \frac{1}{m^2 n^2 (m^2 - 4)(n^2 - 4) [\pi^4(m^2\beta^2 + n^2)^2 + \sigma^2]} \quad (9)$$

$$F_d = \frac{-256\delta\sigma}{\pi^2} \sum_{m,n \in \text{odd}} \frac{m^2\beta^2 + n^2}{m^2 n^2 (m^2 - 4)(n^2 - 4) [\pi^4(m^2\beta^2 + n^2)^2 + \sigma^2]} \quad (10)$$

where ‘ σ ’ is the squeeze number ($\sigma = \frac{12\mu\omega W^2}{p_a h_a^2}$), and β is the aspect ratio ($\beta = \frac{W}{L}$). Similarly, we have obtained expressions for P , F_s and F_d corresponding to all other boundary conditions. These expressions are listed in Appendix A.

2.3 Analytical results and discussion

A. Pressure and phase variation at high and low squeeze numbers

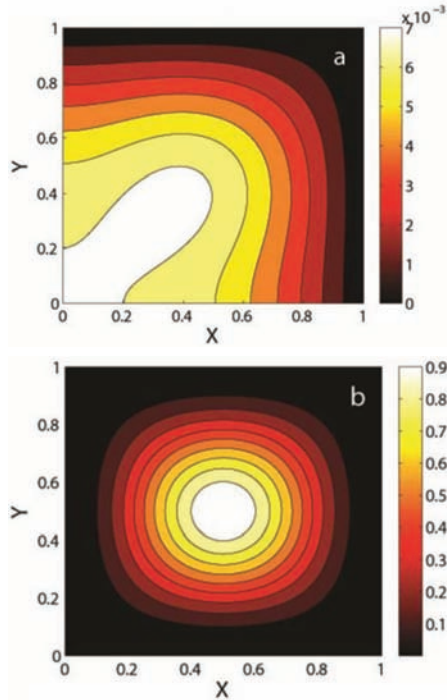


Figure 2: Spatial pressure distribution over the plate for OCCC boundary condition for (a) $\sigma = 0.1$, (b) $\sigma = 1000$

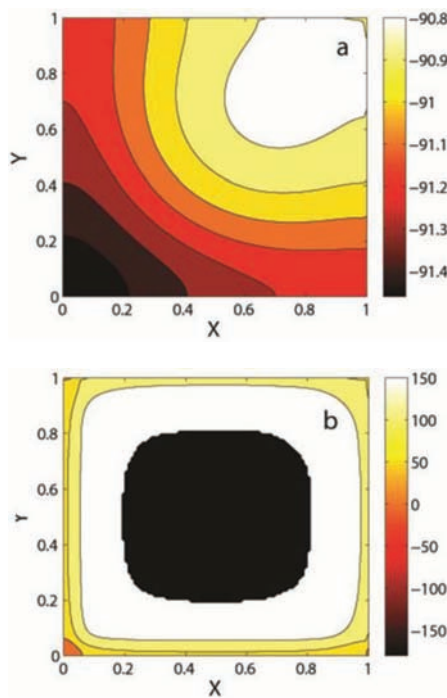


Figure 3: Spatial phase distribution over the plate for OCCC boundary condition for (a) $\sigma = 0.1$, (b) $\sigma = 1000$

Although we have analytical expressions for pressure (and hence spring force and damping force) for all types of flow boundary conditions (see Appendix A); we take OCCC (two adjacent sides open and the other two sides closed) as a representative case here to discuss some salient features of the results obtained. The pressure and the phase angle variation over the entire flow domain for the OCCC boundary conditions are shown in Fig. 2 and Fig. 3, respectively, for two extreme cases of the squeeze number (σ). The squeeze number as defined in section 2.2 is a non dimensional parameter, which is a measure of the fluid compressibility. A detailed discussion on the significance of the squeeze number is provided in [Pratap et al. (2007)]. For a given ambient pressure and plate geometry, the squeeze number is directly proportional to the frequency. The figures for $\sigma = 0.1$ and $\sigma = 1000$ are representative of the pressure and the phase variations at low and high frequencies, respectively. As σ increases, the low frequency variation continuously transforms itself into the high frequency response

From Fig. 2(a) and 2(b), we have observed that the flow boundary conditions used on the sides have a dominant effect on the pressure distribution at a low squeeze number. At high squeeze number, the symmetry in the pressure distribution with a peak in the center clearly indicates that the flow boundary conditions have little influence on the pressure distribution. This is to be expected because the interaction between the fluid film underneath the plate and the outside world decreases with an increasing oscillation frequency and at sufficiently high frequencies, the interaction ceases altogether. Similarly, Fig. 3(a) shows that for low σ , the phase angle is -90° almost everywhere. However, at high σ (Fig. 3(b)), the phase angle reaches -180° over a large portion of the plate.

B. A comparative study of the stiffness and the damping for various flow boundary conditions.

We have plotted the non-dimensional stiffness and the damping coefficients against σ for all boundary conditions in Fig. 4. We noted that at low squeeze numbers the stiffness increases with squeeze number for all venting conditions other than the all sides closed case (CCCC) and approaches the constant stiffness value (non-dimensional value of $1/4$) for the all sides closed case.

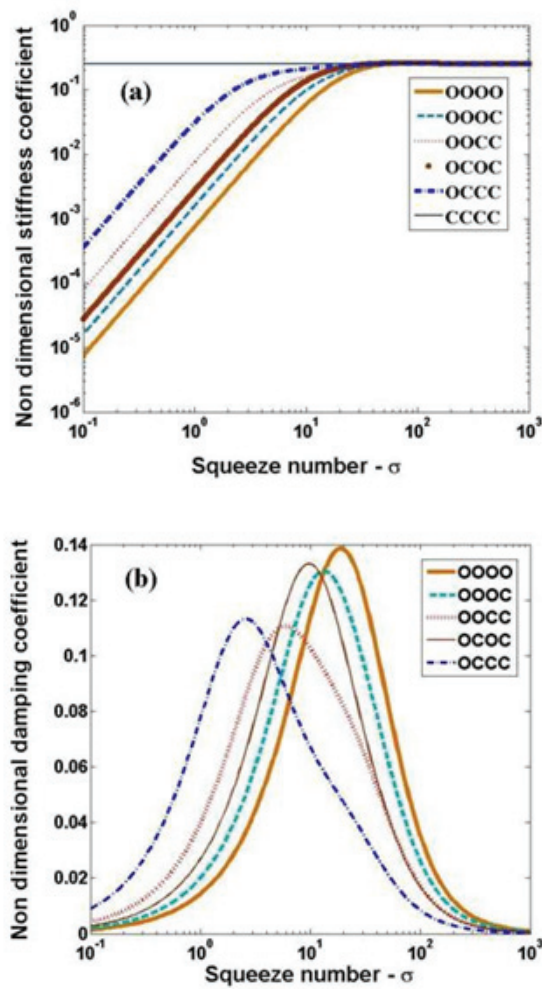


Figure 4: Non-dimensional quantities vs squeeze number for all flow boundaries, (a) stiffness, (b) damping

The damping coefficient at first increases, but subsequently decreases after a critical squeeze number at each venting condition. For the CCCC case, it is zero. In order to investigate these variations further, a comparative study of the stiffness and the damping is carried out. With the all sides open case (OOOO) as the reference, the stiffness and the damping ratios are evaluated for all venting scenarios and plotted against the squeeze number in Fig. 5. We focused our study on the variation of the stiffness and the damping with (a) the increase in the amount of flow restrictions and (b) the relative positions of the restricted flow boundaries. It is observed from Fig. 5 that the OCCC case offers the highest stiffness, which is found to be more than 45 times the OOOO value at low squeeze numbers ($\sigma < 1$). With a decreasing number of restricted boundaries the relative stiffness decreases. At higher squeeze numbers ($\sigma > 100$), the non dimensional stiffness for all the flow scenarios reach the same limiting non-dimensional value of 1/4 which is the constant value for the CCCC case.

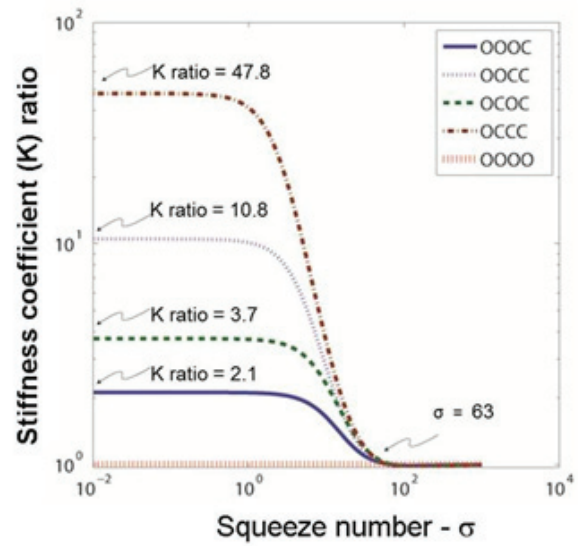


Figure 5: Stiffness coefficient ratio of each venting condition with respect to the all sides open case vs squeeze number

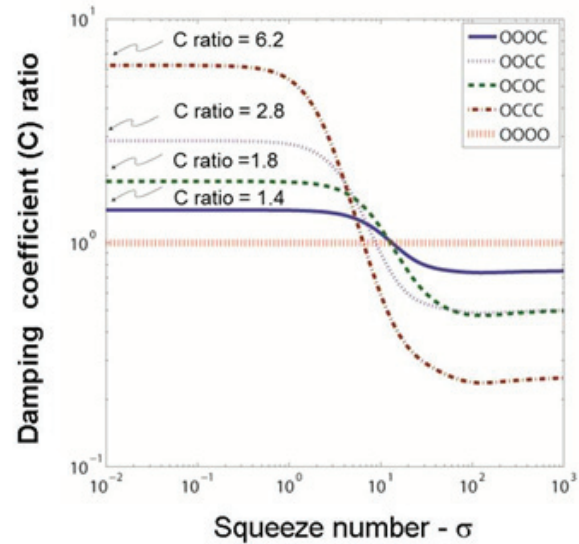


Figure 6: Damping coefficient ratio of each venting conditions with respect to the all sides open case vs squeeze number

The analytical findings for the damping evoke more intrigue as we find the OCCC case to have (see Fig. 6) more than six times the damping; relative to the OOOO case at low squeeze numbers. This result appears counter-intuitive as the OOOO case has lesser degree of flow restrictions and; hence, should have more flow and; consequently, higher fluid damping. At higher squeeze numbers ($\sigma > 100$); however, the OOOO case shows higher damping as is evident from Fig. 4.

The relative variation of the stiffness coefficient is also of importance in the design of MEMS devices, where any change in the structural resonant frequency due to the added stiffness of the squeeze film must be taken into account. This exercise is crucial in those cases where the structural stiffness may be comparable to the

squeeze film stiffness. This is likely to be the case with extremely thin membranes with thicknesses of the order of a few tens of nano meters or even a few nanometer as in the case of graphene. The damping coefficient variation with respect to the squeeze number (see Fig. 4(b)) shows a left shift in the peak with an increase in the flow restrictions. On investigating, we found that the peak squeeze numbers match closely with the corresponding cut off squeeze numbers (σ value where the stiffness and damping curves intersect) for each of the corresponding flow boundary conditions. The peak σ values from Fig. 4(b) for the two extreme flow boundary cases are $\sigma_{OOOO} = 19.05$ and $\sigma_{OCCC} = 2.512$ for OOOO and OCCC cases, respectively. Thus we observed that by changing the flow boundary conditions, the cut off squeeze number changes by more than 85%. This is of significant importance to the MEMS designers, as damping value affects the Q factor as well as the resonant frequency of the vibrating MEMS devices.

C. The effect of relative position of the closed boundaries on the squeeze film damping and the stiffness

We will now try to understand the role of the relative position of the open and closed boundaries on the squeeze film stiffness and damping. We have compared two very similar cases ‘OCCC’ and ‘OCOC,’ which differ only in the relative position of the closed boundaries. It is found that the ‘OCCC’ case offers about 3 times the stiffness of ‘OCOC’ (see Fig. 5) at low values of squeeze number ($\sigma < 1$). At higher squeeze numbers ($\sigma > 100$), the same non-dimensional limiting stiffness value of $1/4$ is reached by both the configurations as seen in Fig. 4. We also found that the ‘OCCC’ case offers about 1.5 times the damping offered (see Fig. 6) by the ‘OCOC’ case at low squeeze numbers ($\sigma < 1$). At higher squeeze numbers both the cases have almost the same damping value (see Fig. 4b). The above observations may be explained by studying the pressure and the phase variation for the different boundary conditions at low and high squeeze numbers. The magnitude of the spring and the damping forces depend upon the cosine and sine components of the total force, respectively. The total force in turn is found out by integrating pressure over the plate area. From the pressure plots of OCOC and OCCC (see Fig. 7) we found that for low squeeze number ($\sigma = 0.1$), a larger flow distance from the highest pressure zone to the boundaries exists in the OCCC case; consequently, leading to more flow and; hence, a higher damping value as mentioned earlier. For a higher value of squeeze number ($\sigma = 1000$), the pressure distribution for the two cases is comparable and the damping is predictably the same. The OCCC pressure distribution

also shows a larger area of higher magnitude than the OCOC case, which leads to a greater net resultant force and; consequently, a higher stiffness coefficient at low squeeze number ($\sigma = 0.1$). For higher squeeze numbers the pressure distribution is more or less the same and the stiffness coefficient has a constant value regardless of the flow boundary conditions. Thus we can see that the relative positions of the closed boundary has a role to play in determining the squeeze film stiffness and the damping; irrespective of the length of the open flow boundary (the same for both OCOC and OCCC).

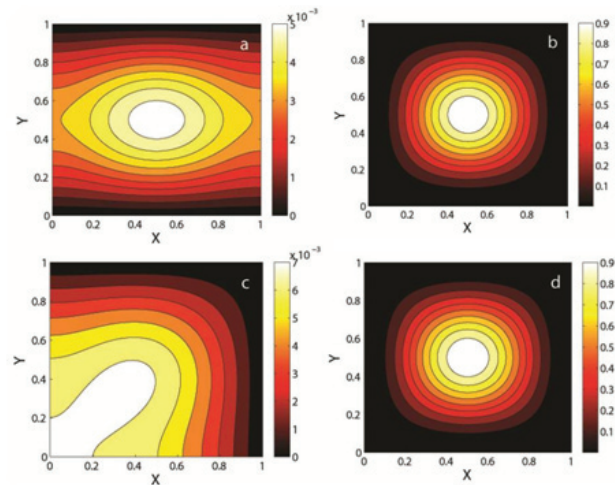


Figure 7: Spatial pressure distribution for OCOC and OCCC boundary conditions for (a) OCOC at $\sigma = 0.1$, (b) OCOC at $\sigma = 1000$, (c) OCCC at $\sigma = 0.1$, (d) OCCC at $\sigma = 1000$

D. The combined effect of the phase angle and the pressure distribution on the squeeze film forces

We have tried to see the effect of the phase angle in combination with the pressure distribution on the squeeze film damping and the stiffness forces. For this purpose, we took the following two extreme scenarios, i.e., the all sides open (OOOO) and the one side open (OCCC) flow boundary cases. From the pressure distribution plots for OOOO and OCCC (Fig. 8), we observed that for a low squeeze number ($\sigma = 0.1$), the pressure gradient for OCCC is higher than that for OOOO. We also noted that for a high squeeze number ($\sigma = 1000$), the pressure profile is almost the same. The higher pressure gradient leads to a higher internal flow for the OCCC case, leading to a higher fluid damping at low squeeze numbers. At higher squeeze numbers, the pressure profile for both the cases are similar, but a higher damping is observed for the OOOO case. A close inspection of the phase distribution at higher squeeze numbers (Fig. 9), show a slight variation in the phase angle at the edges. The OCCC case has slightly lower phase angle values at the corners as compared to the OOOO case; leading to a lower magnitude of the

E. The combined effect of the phase angle and the pressure distribution on the squeeze film forces

We have tried to see the effect of the phase angle in combination with the pressure distribution on the squeeze film damping and the stiffness forces. For this purpose, we took the following two extreme scenarios, i.e., the all sides open (OOOO) and the one side open (OCCC) flow boundary conditions. From the pressure distribution plots for OOOO and OCCC (Fig. 8), we observed that for a low squeeze number ($\sigma = 0.1$), the pressure gradient for OCCC is higher than that for OOOO. We also noted that for a high squeeze number ($\sigma = 1000$), the pressure profile is almost the same. The higher pressure gradient leads to a higher internal flow for the OCCC case, leading to a higher fluid damping at low squeeze numbers. At higher squeeze numbers, the pressure profile for both the cases are similar, but a higher damping is observed for the OOOO case. A close inspection of the phase distribution at higher squeeze numbers (Fig. 9), show a slight variation in the phase angle at the edges. The OCCC case has slightly lower phase angle values at the corners as compared to the OOOO case; leading to a lower magnitude of the damping force (the sine component of the total force contributes to the damping). For a low squeeze number ($\sigma = 0.1$); we can see from Fig. 8 that the OCCC case has a larger region of higher pressure, resulting in a higher magnitude of the total force on the vibrating plate.

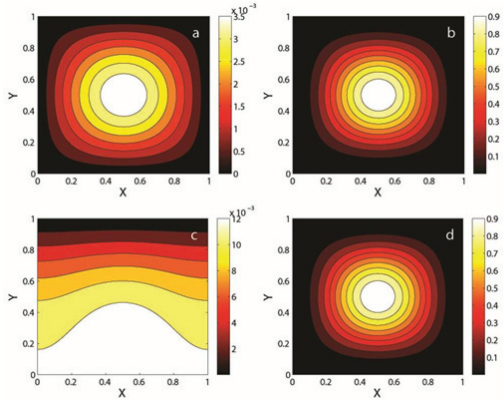


Figure 8: Spatial pressure distribution for OOOO and OCCC boundary conditions for (a) OOOO at $\sigma = 0.1$, (b) OOOO at $\sigma = 1000$, (c) OCCC at $\sigma = 0.1$, (d) OCCC at $\sigma = 1000$

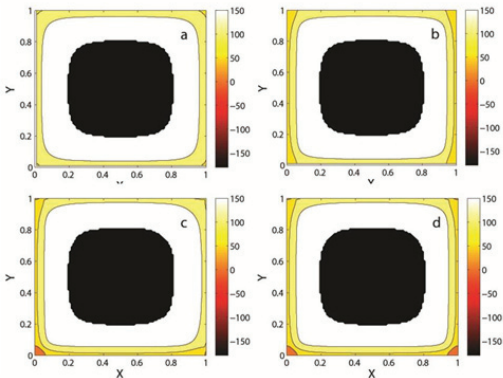


Figure 9: Spatial distribution of phase angle at $\sigma = 1000$ for (a) OOOO, (b) OOCOC, (c) OOOCC and (d) OOOCC boundary conditions

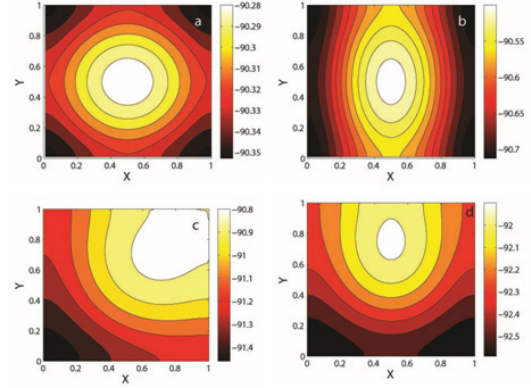


Figure 10: Spatial distribution of phase angle at $\sigma = 0.1$ for (a) OOOO, (b) OOCOC, (c) OOOCC and (d) OOOCC boundary conditions

This results in a higher contribution to the spring force as compared to the OOOO case. At higher squeeze numbers, the pressure profiles are almost the same for all the cases and; hence, each of them reach the same limiting value for the stiffness coefficient. We also noted that the stiffness and the damping values not only vary due to the variation in the pressure distribution for the different flow boundary conditions, but also due to the variation in the phase angle. However, from the plots of the phase distribution (see Figs. 9 and 10) for the different flow boundary conditions; we observed that the phase distribution does not vary as much as the pressure for the different flow restrictions for any given squeeze number. Hence, variation in the stiffness and the damping are largely due to the variation in the pressure distribution.

3 Numerical validation

In order to validate our analytical solutions, we compared them with our numerical finite element based model, which is validated with the experimental results from the literature [Pandey and Pratap (2007)].

3.1 Mathematical formulation

The numerical problem at hand involves the coupled solution of the 2D Reynolds equation for the squeeze film (see Eq. 11) and the 3D elasticity equation (see Eq. 12).

The linearized Reynolds equation is given as follows [Pratap et al.(2007)]:

$$\frac{h_a^3}{12\mu_{eff}} \left(\frac{\partial^2 \hat{p}}{\partial x^2} + \frac{\partial^2 \hat{p}}{\partial y^2} \right) = \frac{h_a}{P_a} \frac{\partial \hat{p}}{\partial t} + \frac{\partial \hat{h}}{\partial t} \quad (11)$$

where μ_{eff} is the effective viscosity, h_a is the initial air gap, P_a is the ambient air pressure, \hat{p} is the fluid pressure (perturbed about P_a) and \hat{h} is the air gap (perturbed about h_a). The last term on the right hand side of the above equation couples the structure and the fluid domain. We can write the variational statement for

the dynamic structural problem without any body force as (refer Appendix B):

$$\int_{\Omega} \boldsymbol{\tau}(\mathbf{u}): \boldsymbol{\varepsilon}(\mathbf{u}_{\delta}) d\Omega + \int_{\Omega} \rho \ddot{\mathbf{u}} \mathbf{u}_{\delta} d\Omega = \int_{\Gamma_t} \mathbf{u}_{\delta} \cdot \bar{\mathbf{t}} d\Gamma \quad (12)$$

where ρ is the density, \mathbf{u} is the displacement, \mathbf{u}_{δ} is its variation, $\boldsymbol{\tau}$ is the stress, $\bar{\mathbf{t}}$ is the prescribed traction over the boundary Γ_t and $\boldsymbol{\varepsilon}(\mathbf{u}_{\delta})$ is given by (13):

$$\boldsymbol{\varepsilon}(\mathbf{u}_{\delta}) = \frac{1}{2} [(\nabla \mathbf{u}_{\delta}) + (\nabla \mathbf{u}_{\delta})^T] \quad (13)$$

$$\boldsymbol{\tau}(\mathbf{u}): \boldsymbol{\varepsilon}(\mathbf{u}_{\delta}) = \tau_{ij}(\mathbf{u}): \varepsilon_{ij}(\mathbf{u}_{\delta}) \quad (14)$$

with the summation convention over repeated indices.

The traction term in Eq.(12) is $\int_{\Gamma} [\mathbf{u}_{\delta}(\bar{\mathbf{t}})] d\Gamma$. We can model the squeeze film pressure on the “wet” surface as a prescribed traction, $\mathbf{t}_{wet} = -(\hat{\mathbf{p}})\hat{\mathbf{n}}$ where $\hat{\mathbf{n}}$ denotes the outward normal for the wet surface. We can also actuate the structure electrostatically, model this force as an electrostatic traction \mathbf{t}_{el} , acting on the top surface of the vibrating plate. Next we can write the prescribed traction from the squeeze film pressure as $-\int_{\Gamma_{wet}} [\hat{\mathbf{p}}\mathbf{u}_{\delta}\hat{\mathbf{n}}]$. Incorporating all the prescribed tractions as described and dropping the subscript for \mathbf{t}_{el} , we can rewrite Eq. (12) as follows:

Incorporating all the prescribed tractions as described and dropping the subscript for \mathbf{t}_{el} , we can rewrite Eq. (12) as follows:

$$\int_{\Omega} \boldsymbol{\tau}(\mathbf{u}): \boldsymbol{\varepsilon}(\mathbf{u}_{\delta}) d\Omega + \int_{\Omega} \rho \ddot{\mathbf{u}} \mathbf{u}_{\delta} d\Omega + \int_{\Gamma_{wet}} \hat{\mathbf{p}} \mathbf{u}_{\delta} \cdot \hat{\mathbf{n}} d\Gamma = \int_{\Gamma_t} \mathbf{u}_{\delta} \cdot (\bar{\mathbf{t}}) d\Gamma \quad (15)$$

Using the procedure outlined in our prior work [Roychowdhury et al. (2013)], we discretized the fluid and the structural equations using the 27 node 3D elements to model the structure, and the 9 node 2D elements to model the “wet” fluid interface. After the finite element discretization, we arrived at the following coupled formulation:

$$\begin{bmatrix} \mathbf{K}_{uu} & \mathbf{K}_{up} \\ \mathbf{K}_{pu} & \mathbf{K}_{pp} \end{bmatrix} \begin{Bmatrix} \hat{\mathbf{u}} \\ \hat{\mathbf{p}} \end{Bmatrix} = \begin{Bmatrix} \mathbf{f}_u \\ \mathbf{0} \end{Bmatrix} \quad (16)$$

where the stiffness matrices are as follows:

$$\mathbf{K}_{uu} = -\omega^2 \mathbf{M}_u + \mathbf{K}_u$$

$$\mathbf{M}_u = \int_{\Omega} \rho \mathbf{N}_u^T \mathbf{N}_u d\Omega$$

$$\mathbf{K}_u = \int_{\Omega} \mathbf{B}_u^T \mathbf{C} \mathbf{B}_u d\Omega$$

$$\mathbf{K}_{up} = \int_{\Gamma_{wet}} \mathbf{N}_u^T \hat{\mathbf{n}} \mathbf{N}_p d\Gamma$$

$$\mathbf{f}_u = \int_{\Gamma_t} \mathbf{N}_u^T \bar{\mathbf{t}} d\Gamma$$

$$\mathbf{K}_{pp} = \frac{(h_a^3)}{12\mu_{eff}} \int_{\Gamma_{wet}} \mathbf{B}_p^T \mathbf{B}_p d\Gamma + \frac{j\omega h_a}{P_a} \int_{\Gamma_{wet}} \mathbf{N}_p^T \mathbf{N}_p d\Gamma$$

$$\mathbf{K}_{pu} = j\omega \int_{\Gamma_{wet}} \mathbf{N}_p^T \mathbf{N}_p \mathbf{u}_z d\Gamma$$

In the above expressions, ω is the angular excitation frequency, ρ is the density of the air, $\mathbf{N}_u, \mathbf{N}_p$ are the shape function matrices for the displacement and the pressure respectively, $\mathbf{B}_u, \mathbf{B}_p$ are the strain displacement matrices for the displacement and the pressure respectively, $\bar{\mathbf{t}}$ represents the prescribed traction, h_a is the initial air gap, μ_{eff} is the effective viscosity of the air and P_a is the ambient air pressure.

3.2 Validation of the numerical model with the experimental results

We validated our numerical results with the published experimental data for a cantilever beam subjected to electrostatic actuation [Pandey and Pratap (2007)]. The numerically obtained quality factors (Q) for the first three modes of vibration of the specified beam is compared with the reported experimental data. The beam dimensions and the fluid parameter values are taken in accordance with those reported in the work by [Pandey and Pratap (2007)]. In our simulations, we have subjected the cantilever to a sinusoidal voltage of 1.5 V, which is well below the pull-in voltage of 6 V for the given cantilever. The input voltage has been applied as an electrostatic pressure load of magnitude 5.08 N/m² in our FEM model for the cantilever beam; considering a parallel plate capacitor with a small displacement approximation [Saucedo et al.(2003)]. The beam tip velocities have been obtained from the simulations, normalized with respect to the applied voltage and plotted against frequency.

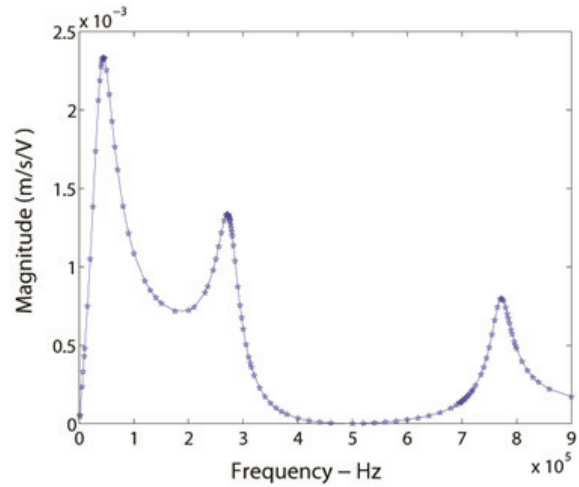


Figure 11: Numerically obtained frequency response of a poly Si cantilever beam of length 350 μm , width 22 μm and thickness 4 μm

Q factors for different modes are obtained using the half power method from the frequency response. The frequency response so obtained is shown in Fig. 11. The plot shows three distinct peaks corresponding to the first three modes, and is in close agreement with a similar plot reported by [Pandey and Pratap (2007)].

Tab.1. shows the comparative results for the Q factor. The simulations have been run with a converged mesh, the details of which we have reported in our prior work [Roychowdhury et al. (2013)].

Table 1. Q factor comparison for the first three modes of a cantilever beam of length $350\mu\text{m}$, width $22\mu\text{m}$.

Mode	Q _{exp}	Q _{FEM}
1	1.20	1.095
2	7.58	5.849
3	18.5	20.379

3.3 Comparison of the numerical model with analytical solutions

We compared our analytical solutions with results from our numerical model. We took two representative cases for comparison, namely the all sides open case “OOOO” and the opposite sides open case “OCOC”. We used a 4×4 mesh of 27 node brick elements for FEM modeling of the plate. In order to compare our FEM results with the analytical solutions, we used the approximate first mode shape of the plate chosen as a prescribed displacement for our numerical model.

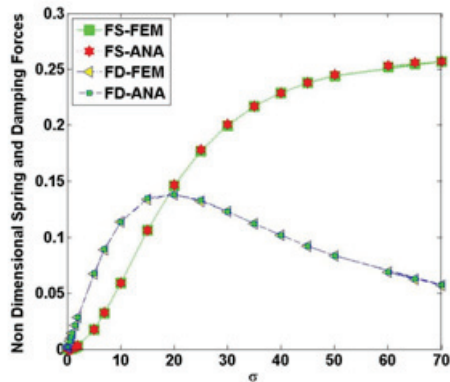


Figure 11: Numerical and analytically obtained spring and damping forces vs squeeze number (σ) for “OOOO” configuration for a square plate.

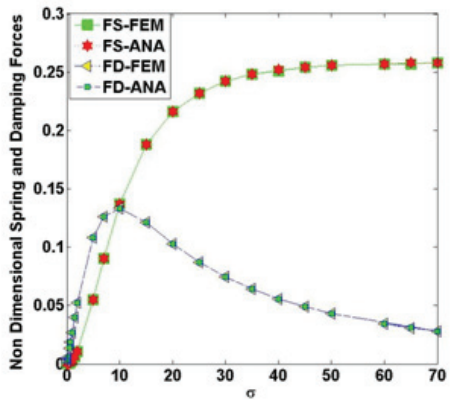


Figure 12: Numerical and analytically obtained spring and damping forces vs squeeze number (σ) for “OCOC” configuration for a square plate.

The resulting pressure distribution is integrated over the wet surface to get the force on the vibrating plate. The squeeze film spring (F_s) and the damping (F_d) forces are obtained from the real and the imaginary component of the resultant force, respectively. The forces are non-dimensionalised and plotted against a non dimensional parameter squeeze number σ , that is directly related to the frequency of harmonic excitation as follows. Fig. 12 shows the plots for F_s and F_d for the “OOOO” case, and Fig. 13 shows the same for the “OCOC” case. We observed from these plots that the numerical stiffness and the damping forces are in close agreement with the analytical results for both the flow boundary cases studied. The two methods also show a good agreement at both high and low squeeze numbers (σ) (thus high and low frequencies). The deviation between the numerical and analytical results have been found to be less than 2% for both the flow boundary conditions studied. Thus our numerical results show a good agreement with the analytical solutions.

3.4 Limitations of the current model

The analytical model discussed in this work, accounts for the plate elasticity by using an approximate first mode shape as an input to the model. The subsequent calculations are based on only the first structural mode shape. For all motions that have a combination of mode shapes involved, the results presented here will not be directly applicable. Thus the idea of tuning the Q of the structure with an appropriate design of the flow boundary conditions is limited to the structural oscillations dominated by the first mode.

4 Conclusions

In this work, we have discussed how variations in the flow boundaries may be used as a tool to tune the squeeze film stiffness and the damping of vibratory MEMS devices. We have presented an analytical solution for the squeeze film problem for the elastic rectangular micro-plates based on an eigen expansion method, and compared our results with the finite element based numerical solutions to the coupled Reynolds equation and the 3D elasticity equation, which we have reported in a prior work. From the analytical results, we found that at high frequencies of oscillation the pressure profile follows the displacement profile of the plate and is thus, independent of the flow boundary conditions. Also, the phase angle varies from 90° to 180° from low frequencies to high frequencies as a consequence of, which the spring force dominates at high frequencies and the damping force dominates at low frequencies. For the closed cavity case we found damping to be nonexistent, and we also noted that the

stiffness coefficient is a constant for a given pressure value.

We have investigated the variations in the damping and the spring force due to both the orientation of the closed boundaries (i.e., two adjacent sides closed versus two opposite sides closed), and the number of flow restricted boundaries. We found out that for low squeeze numbers ($\sigma < 1$), the pressure gradient plays a key role in determining the damping as internal flow due to this gradient results in a higher than expected damping in the more restricted cases. We also found that at low squeeze numbers ($\sigma < 1$), the more restricted boundary conditions lead to higher stiffness. The OCCC configuration is found to have about 45 times the stiffness of the OOOO case. From the analytical results, at high squeeze numbers it is observed that the stiffness coefficient reaches a constant limiting value irrespective of the flow boundary conditions; whereas the damping coefficient values vary relative to the number of closed boundaries, their orientation having no significant effect. The analytical results show a good

agreement with our FEM based solutions, and thus can be used with confidence in design calculations to evaluate damping easily. The above knowledge can be utilized in designing different flow boundary conditions for circular cases; where it is easier to control the flow boundary restriction along the circumference, and thus resulting in greater control on the change of the squeeze film stiffness and the damping. We thus studied the use of different venting conditions as a design tool in modifying the squeeze film induced stiffness and damping, and thus found out the Q factor for a vibratory MEMS system.

Acknowledgement

The authors would like to acknowledge Prof. C.S. Jog of the Department of Mechanical Engineering, Indian Institute of Science (IISc), Bangalore and NPMAS grant for the computational micro-systems. The authors also acknowledge the support from CoNE Lab of the Center for Nano Science and Engineering at IISc.

APPENDIX A

Table 2. Analytical expressions for squeeze film forces and pressure for all sides open (OOOO) case.

BC	Non - Dimensional Quantities
"OOOO"  $\bar{P}(0, y) = \bar{P}(L, y) = 0$ $\bar{P}(x, 0) = \bar{P}(x, W) = 0$	$\bar{P} = -64\delta \sum_{m,n \in \text{odd}} \frac{[i\pi^2\sigma(m^2\beta^2 + n^2) + \sigma^2] \sin\left(\frac{m\pi x}{L}\right) \sin\left(\frac{n\pi y}{W}\right)}{[\pi^4(m^2\beta^2 + n^2)^2 + \sigma^2]mn\pi^2(m^2 - 4)(n^2 - 4)}$ $F_s = -\frac{256\delta\sigma^2}{\pi^4} \sum_{m,n \in \text{odd}} \frac{1}{m^2n^2(m^2 - 4)(n^2 - 4)[\pi^4(m^2\beta^2 + n^2)^2 + \sigma^2]}$ $F_d = -\frac{256\delta\sigma}{\pi^2} \sum_{m,n \in \text{odd}} \frac{m^2\beta^2 + n^2}{[\pi^4(m^2\beta^2 + n^2)^2 + \sigma^2]m^2n^2(m^2 - 4)(n^2 - 4)}$

Table 3. Analytical expressions for squeeze film forces and pressure for one side closed (OOOC) case.

BC	Non - Dimensional Quantities
"OOOC"  $\frac{\partial \bar{P}}{\partial x}(0, y) = \bar{P}(L, y) = 0$ $\bar{P}(x, 0) = \bar{P}(x, W) = 0$	$\bar{P} = -256\delta \sum_{m,n \in \text{odd}} \frac{(-1)^{\frac{m-1}{2}} [i\pi^2\sigma\left(\frac{m^2\beta^2}{4} + n^2\right) + \sigma^2]}{[\pi^4\left(\frac{m^2\beta^2}{4} + n^2\right)^2 + \sigma^2]mn\pi^2(m^2 - 16)(n^2 - 4)}$ $\times \cos\left(\frac{m\pi x}{2L}\right) \sin\left(\frac{n\pi y}{W}\right)$ $F_s = -\frac{1024\delta\sigma^2}{\pi^4} \sum_{m,n \in \text{odd}} \frac{1}{m^2n^2(m^2 - 16)(n^2 - 4)[\pi^4\left(\frac{m^2\beta^2}{4} + n^2\right)^2 + \sigma^2]}$ $F_d = -\frac{1024\delta\sigma}{\pi^2} \sum_{m,n \in \text{odd}} \frac{\frac{m^2\beta^2}{4} + n^2}{[\pi^4\left(\frac{m^2\beta^2}{4} + n^2\right)^2 + \sigma^2]m^2n^2(m^2 - 16)(n^2 - 4)}$

Table 4. Analytical expressions for squeeze film forces and pressure for one side closed (OOOC) case.

BC	Non - Dimensional Quantities
"OOOC" 	$\bar{P} = -1024\delta \sum_{m,n \in \text{odd}} \frac{(-1)^{\frac{m+n-2}{2}} [4i\pi^2\sigma(m^2\beta^2 + n^2) + 16\sigma^2]}{[\pi^4(m^2\beta^2 + n^2)^2 + 16\sigma^2]mn\pi^2(m^2 - 16)(n^2 - 16)}$ $\times \cos\left(\frac{m\pi x}{2L}\right) \sin\left(\frac{n\pi y}{2W}\right)$ $F_s = -\frac{65536\delta\sigma^2}{\pi^4} \sum_{m,n \in \text{odd}} \frac{1}{m^2n^2(m^2 - 16)(n^2 - 16)[\pi^4(m^2\beta^2 + n^2)^2 + 16\sigma^2]}$ $F_d = -\frac{16384\delta\sigma}{\pi^2} \sum_{m,n \in \text{odd}} \frac{m^2\beta^2 + n^2}{[\pi^4(m^2\beta^2 + n^2)^2 + 16\sigma^2]m^2n^2(m^2 - 16)(n^2 - 16)}$
$\frac{\partial \bar{P}}{\partial x}(0, y) = \frac{\partial \bar{P}}{\partial x}(L, y) = 0$ $\frac{\partial \bar{P}}{\partial y}(x, 0) = \frac{\partial \bar{P}}{\partial y}(x, W) = 0$	

Table 5. Analytical expressions for squeeze film forces and pressure for two adjacent sides closed (OOCOC) case.

BC	Non - Dimensional Quantities
"OOCOC" 	$\bar{P} = 4\delta \sum_{n \in \text{odd}} \frac{1}{n\pi(n^2 - 4)} \sin\left(\frac{n\pi y}{W}\right)$ $\times \left[\frac{i\sigma\pi^2n^2 + \sigma^2}{\pi^4n^4 + \sigma^2} - \frac{i\sigma\pi^2(4\beta^2 + n^2) + \sigma^2}{\pi^4(4\beta^2 + n^2)^2 + \sigma^2} \right] \cos\left(\frac{2\pi x}{L}\right)$ $F_s = \frac{8\delta\sigma^2}{\pi^2} \sum_{n \in \text{odd}} \frac{1}{n^2(n^2 - 4)[\pi^4n^4 + \sigma^2]}$ $F_d = 8\delta\sigma \sum_{n \in \text{odd}} \frac{1}{[\pi^4n^4 + \sigma^2](n^2 - 4)}$
$\frac{\partial \bar{P}}{\partial x}(0, y) = \frac{\partial \bar{P}}{\partial x}(L, y) = 0$ $\bar{P}(x, 0) = \bar{P}(x, W) = 0$	

Table 6. Analytical expressions for squeeze film forces and pressure for three sides closed (OCCC) case.

BC	Non - Dimensional Quantities
"OCCC" 	$\bar{P} = 64\delta \sum_{n \in \text{odd}} \frac{(-1)^{\frac{n-1}{2}}}{n\pi(n^2 - 16)} \cos\left(\frac{n\pi y}{2W}\right)$ $\times \left[\frac{i\sigma\pi^2n^2 + 4\sigma^2}{\pi^4n^4 + 16\sigma^2} - \frac{i\sigma\pi^2(16\beta^2 + n^2) + 16\sigma^2}{\pi^4(16\beta^2 + n^2)^2 + 16\sigma^2} \right] \cos\left(\frac{2\pi x}{L}\right)$ $F_s = \frac{512\delta\sigma^2}{\pi^2} \sum_{n \in \text{odd}} \frac{1}{n^2(n^2 - 16)[\pi^4n^4 + 16\sigma^2]}$ $F_d = 128\delta\sigma \sum_{n \in \text{odd}} \frac{1}{[\pi^4n^4 + 16\sigma^2](n^2 - 16)}$
$\frac{\partial \bar{P}}{\partial x}(0, y) = \frac{\partial \bar{P}}{\partial x}(L, y) = 0$ $\frac{\partial \bar{P}}{\partial y}(x, 0) = \bar{P}(x, W) = 0$	

Table 7. Analytical expressions for squeeze film forces and pressure for all sides closed (CCCC) case.

BC	Non - Dimensional Quantities
"CCCC" 	$\bar{P} = -\frac{\delta}{4} \left[1 - \frac{\sigma^2 + 4i\pi^2\sigma}{\sigma^2 + 16\pi^4} \cos\left(\frac{2\pi y}{W}\right) - \frac{\sigma^2 + 4i\pi^2\sigma\beta^2}{(\sigma^2 + 16\pi^4)\beta^4} \cos\left(\frac{2\pi x}{L}\right) \right]$ $+ \frac{\sigma^2 + 4i\pi^2\sigma(1 + \beta^2)}{[16\pi^4(1 + \beta^2)^2 + \sigma^2]} \cos\left(\frac{2\pi x}{L}\right) \cos\left(\frac{2\pi y}{W}\right)$ $F_s = \frac{-\delta}{4}$ $F_d = 0$
$\frac{\partial \bar{P}}{\partial x}(0, y) = \frac{\partial \bar{P}}{\partial x}(L, y) = 0$ $\frac{\partial \bar{P}}{\partial y}(x, 0) = \frac{\partial \bar{P}}{\partial y}(x, W) = 0$	

APPENDIX B

The derivation for the variational statement for the dynamic structural problem is provided below. We have the equation of motion as [da Silva (2006)],

$$\rho \ddot{\mathbf{u}} = \nabla \cdot \boldsymbol{\tau} + \mathbf{b} \quad (\text{B1})$$

Where ‘ ρ ’ is the density of the structure and ‘ \mathbf{b} ’ represents the body force per unit volume. We have obtained the variational formulation using the method of weighted residuals, based on the equilibrium equation and the natural boundary conditions as follows:

$$\int_{\Omega} \mathbf{u}_{\delta} \cdot (\nabla \cdot \boldsymbol{\tau} + \mathbf{b} - \rho \ddot{\mathbf{u}}) + \int_{\Gamma_t} \mathbf{u}_{\delta} \cdot (\bar{\mathbf{t}} - \mathbf{t}) d\Gamma = 0 \quad (\text{B2})$$

where $\bar{\mathbf{t}}$ represents the prescribed tractions. Now using the tensor identity

$$\nabla \cdot (\boldsymbol{\tau}^t \mathbf{u}_{\delta}) = \mathbf{u}_{\delta} \cdot (\nabla \cdot \boldsymbol{\tau}) + \nabla(\mathbf{u}_{\delta}) : \boldsymbol{\tau} \quad (\text{B3})$$

we can rewrite Eq. (B2), without the body force term as:

$$\int [\nabla \cdot (\boldsymbol{\tau}^t \mathbf{u}_{\delta}) - \nabla(\mathbf{u}_{\delta}) : \boldsymbol{\tau} - \rho \ddot{\mathbf{u}}] d\Omega + \int_{\Gamma_t} \mathbf{u}_{\delta} \cdot (\bar{\mathbf{t}} - \mathbf{t}) d\Gamma = 0 \quad (\text{B4})$$

Now applying the divergence theorem to the first term of Eq. (B4), we have the following:

$$\int_{\Gamma} [(\boldsymbol{\tau}^t \mathbf{u}_{\delta}) \cdot \hat{\mathbf{n}}] d\Gamma - \int_{\Omega} [\nabla \mathbf{u}_{\delta} : \boldsymbol{\tau} + \mathbf{u}_{\delta} \rho \ddot{\mathbf{u}}] d\Omega + \int_{\Gamma_t} \mathbf{u}_{\delta} \cdot (\bar{\mathbf{t}} - \mathbf{t}) d\Gamma = 0 \quad (\text{B5})$$

Now using Cauchy relations ($\mathbf{t} = \tau \hat{\mathbf{n}}$) on Γ and the fact that $\mathbf{u}_{\delta} = 0$ on Γ_u (specified displacement domain), the first integral from Eq. (B5) is modified as:

$$\int_{\Gamma} [(\boldsymbol{\tau}^t \mathbf{u}_{\delta}) \cdot \hat{\mathbf{n}}] d\Gamma = \int_{\Gamma_t} \mathbf{u}_{\delta} \cdot \bar{\mathbf{t}} d\Gamma \quad (\text{B6})$$

Thus we can rewrite, Eq. (B6) as follows:

$$\int_{\Omega} [\nabla \mathbf{u}_{\delta} : \boldsymbol{\tau}] d\Omega = \int_{\Gamma_t} \mathbf{u}_{\delta} \cdot \bar{\mathbf{t}} d\Gamma - \int_{\Omega} [\mathbf{u}_{\delta} \cdot \rho \ddot{\mathbf{u}}] d\Omega \quad (\text{B7})$$

Eq. (B7) is the variational statement for the dynamic structural problem without body force.

REFERENCES:

- Ahmad, B. and Pratap, R. (2011) Analytical evaluation of squeeze film forces in a CMUT with sealed air-filled cavity, *IEEE Sensors*, Vol. 11, no. 10, pp. 2426-2431.
- Altug, B. M. M. and Rao, M. D. (2010) Analytical modeling of squeeze film damping for rectangular elastic plates using Greens functions, *J. Sound Vibr.*, Vol. 329, no. 22, pp. 4617-4633.
- Blech, J. J. (1983) On isothermal squeeze films, *ASME J. Lubric. Technol.*, Vol. 105, No. 4, pp. 615-620.
- Darling, R., Hivick, C. and Xu, J. (1998) Compact analytical modeling of squeeze film damping with arbitrary venting conditions using a Greens function approach, *Sens. Actuators A*, Vol. 70, No. 1, pp. 32-41.
- Da Silva, (2006) *Mechanics and Strength of Materials*, Springer, Berlin Heidelberg NewYork.
- Kumar, S. (2010) Effect of Squeeze Film Flow on Dynamic Response of MEMS Structures with Restrictive Flow Boundary Conditions. Master’s Thesis, Indian Institute of Science, Bangalore, India.
- Langlois, W. E. (1962) Isothermal squeeze films, *Quart. Appl. Math.*, Vol. XX, No. 2, pp. 131-150.
- Mohite, S. (2005) Study of Squeeze Film Effects in Modelling Dynamic MEMS Device. Ph.D Thesis, Indian Institute of Science, Bangalore, India.
- Pandey, A. K., Pratap, R. and Chau, F. S. (2007) Influence of boundary conditions on the dynamic characteristics of squeeze films in MEMS devices. *J. Micromech. Microeng.*, Vol. 16, No. 4, pp. 893-903.
- Pandey, A. K. and Pratap, R. (2007) Effect of flexural modes on squeeze film damping in MEMS cantilever resonators. *Journal of Micromechanics and Microengineering*, Vol. 17, No. 12, pp. 2475-2484.
- Pratap, R., Mohite S. and Pandey, A. K. (2007) Squeeze film effects in MEMS devices. *Journal of the Indian Institute of Science*, Vol. 87, No. 1, pp. 75-94.
- Roychowdhury, A., Nandy, A., Jog, C.S. and Pratap R. (2013) A monolithic, FEM-based approach for the coupled squeeze film problem of an oscillating elastic micro-plate using 3D 27-node elements. *Journal of Applied Mathematics and Physics*, Vol. 1, No. 6, pp. 20-25.
- Saucedo-Flores, E., Ruelas, R., Florer, M. and Chiao, I. C. (2003) Study of the pull in voltage for MEMS parallel plate capacitor actuators, *Materials Research Society Fall Meeting*, Boston, Dec 1-5, 2003.
- Veijola, T., Kuusma, H., Lahdenperä, J. and Ryhänen, T. (1995) Equivalent-circuit model of the squeezed gas film in a silicon accelerometer, *Sensors and Actuators A. Physical*, Vol. 48, No. 43, pp. 239-248.

Anish Roychowdhury: Anish received his B.E. (Honors)



in Mechanical Engineering from the National Institute of Technology (NIT), Durgapur, India in 2001, and his M.S. degree in Mechanical Engineering from Louisiana State University, USA in 2007.

He has about 6 years of experience as a software developer across various IT MNC's. He is currently working towards a doctoral degree, specializing in MEMS modeling in the Department of Mechanical Engineering and the Center for Nano Science and Engineering at the Indian Institute of Science, Bangalore, India.

Siddhartha Patra: Siddhartha received his B.E. (Honors)



in Mechanical Engineering in 2009 from Jadavpur University, Kolkata, India. He received his M.E. degree in Mechanical Engineering from the Indian Institute of Science, Bangalore, India in 2011. His masters work is based on the effects of

different flow boundary conditions on the squeeze film parameters in MEMS devices. Siddhartha Patra is currently working in Jadavpur University, Kolkata as a faculty member in the Department of Mechanical Engineering. He has nearly three years of working experience in ANSYS Fluent India Pvt. Ltd. as an Application Engineer with an expertise in the fields of Material Non-linearity, large deformation theory and FEA.

Arup Nandy: Arup received his BE. in Mechanical



Engineering from Bengal Engineering and Science University, Shibpur, West Bengal, India in 2009. He got his M.E. degree in Mechanical Engineering in 2011 from IISc, Bangalore, India. He is currently pursuing

Phd in Mechanical Engineering at IISc. He is working in structural optimization, FEM modeling of structural acoustic interaction, structure coupled with squeeze film damping and electromagnetics.

Rudra Pratap: Prof. Rudra Pratap received the B.Tech.



degree from the Indian Institute of Technology, Kharagpur, India, in 1985, Master's degree in mechanics from the University of Arizona, Tucson, in 1987, and the Ph.D. degree in theoretical and applied mechanics from the Cornell

University, Cornell, NY, in 1993. He taught at the Sibley School of Mechanical and Aerospace Engineering, Cornell University during 1993–1996, prior to joining the Indian Institute of Science in 1996. He is currently a Professor with the Department of Mechanical Engineering and the Chairman for the Centre for Nano Science and Engineering, Indian Institute of Science Bangalore, India. His research interests include MEMS design, computational mechanics, nonlinear dynamics, structural vibration, and vibroacoustics. Prof. Pratap is a member of the ISSS and is an Associate Editor of the International Journal of Shock and Vibration.